Circulation and Dynamics of the Western North Atlantic. Part I: Multiscale Feature Models

AVIJIT GANGOPADHYAY,* A. R. ROBINSON, AND H. G. ARANGO+

Division of Applied Sciences, Department of Earth and Planetary Sciences, Harvard University, Cambridge, Massachusetts

(Manuscript received 11 May 1996, in final form 31 January 1997)

ABSTRACT

This is the first part of a three-part study on the circulation, dynamics, and mesoscale forecasting of the western North Atlantic. The overall objective of this series of studies is threefold: 1) to present a methodology for deriving a dynamically balanced regional climatology that maintains the synoptic structure of the permanent fronts embedded in a mean background circulation, 2) to present a methodology for using such a regional climatology for calibrating and validating dynamical models, and 3) to use similarly derived synoptic realizations as initialization and assimilation fields for mesoscale nowcasting and forecasting.

In this paper, a data-based, kinematically balanced circulation model for the western North Atlantic is developed and described. The various multiscale synoptic and general circulation structures in this region are represented by analytical and analytical/empirical functions based on dynamical considerations and using observational datasets. These include the jet-scale currents, namely, the Gulf Stream and the deep western boundary current, the subbasin-scale recirculating gyres called the southern and the northern recirculation gyres, and the slope water gyre. The inclusion of subbasin-scale gyres as the background circulation for the energetic jet and mesoscale activity in any limited oceanic region is a new paradigm of this multiscale regional modeling study. A generalized kinematical constraint that links the multiscale structures is derived in terms of their interaction scales. For synoptic realizations, the currents and gyres are distorted from their mean state with mass conserving constraints, and mesoscale structures are added thereon. The kinematically balanced linked system is then adjusted via quasigeostrophic dynamics and a regional water-mass model to obtain three-dimensional circulation fields to be used for initialization and assimilation in primitive equation models.

1. Introduction

Over the last two decades, knowledge of the actual structures that constitute the circulation and variability of the oceans has accrued, which enables us now to conceptualize a realistic picture of circulation systems. The structure of the synoptic and the mean circulation can be quite different. Structures exist and evolve on many scales, and a characterization of the mean and the synoptic state of a region of the ocean can be represented by a linked set of multiscale ''features.'' The synoptic state of an oceanic region is generally characterized by interacting free currents and vortices embedded in a background circulation. Although the energy of these features comes originally from large-scale atmospheric forcing, much of the detailed synoptic structures arise from internal dynamical processes. Interacting scales include large-scale, subbasin-scale, mesoscale, cross-axis jet-scale, and submesoscale. A conceptualized multiscale structure based circulation system is generic, that is, valid for any oceanic region; each oceanic region, however, requires a specific set of linked circulation structures or features.

To represent the circulation of a particular region, one needs to characterize the structures and to construct the system of linked features that constitute the circulation and its variabilities. The regional multiscale feature model (MSFM) should be made kinematically consistent with respect to mass conservation, that is, mass exchange linkages between the features. It may, additionally, be adjusted to geostrophic and/or higher-order dynamics. Such a circulation model provides a general synthesis of the regional circulation and also serves as an efficient basis to characterize the synoptic state of the region.

Ocean forecasting and realistic data-driven simulations require initialization and assimilation fields, and an efficient representation of synoptic realizations is valuable in this regard. The importance of obtaining a dynamically balanced initial state for forecasts has been

* Current affiliation: Department of Physics, University of Massachusetts—Dartmouth, North Dartmouth, Massachusetts.

+ Current affiliation: IMCS, Rutgers University, New Brunswick, New Jersey.

Corresponding author address: Dr. Avijit Gangopadhyay, Center for Marine Science and Technology, University of Massachusetts—Dartmouth, 706 S. Rodney French Boulevard, New Bedford, MA 02744.
E-mail: avijit@atlantic.cmast.umassd.edu

emphasized by Hurlburt (1986), Hurlburt et al. (1990), Robinson et al. (1988, 1989), Fox et al. (1993), and others. In fact, motivated by such reasoning, the U.S. Navy's Optimum Thermal Interpolation System (OTIS) was developed by Clancy et al. (1990). In contrast to using climatological background fields as in OTIS, which generally are quite different from the synoptic energetic mesoscale features, our approach here constitutes a framework for obtaining efficiently an actual synoptic realization via observations with minimal resource requirements. Another motivation for constructing the multiscale feature models was to develop a parameter-based synoptic regional climatology to validate and calibrate the dynamical models used for mesoscale synoptic dynamical prediction in the western North Atlantic (WNA).

In this study, we deal with the Gulf Stream meander and ring (GSMR) region. We construct velocity-based feature models for the Gulf Stream (GS), the deep western boundary current (DWBC), the northern recirculation gyre (NRG), the southern recirculation gyre (SRG), and the slope water gyre (SLP) from a comprehensive set of observational data and prior synthetical studies. To construct a synoptic realization, the mean features are kinematically linked and distorted with mass conserving constraints. To the synoptically distorted state, mesoscale rings are added, as well as any other information about open-ocean mesoscale structures available from other sources such as satellite data. This kinematical synthesis is quasigeostrophically adjusted with a mean stratification of the region, and the initialization–assimilation fields are then determined by using a regional water-mass model described by Lozano et al. (1996).

We describe the individual feature models in section 2. The kinematic aspects of coupling these features is described in section 3. The synoptic structures of permanent fronts are kinematically synthesized with mean background circulation to yield a regional synoptic climatology, which is discussed in section 4. The construction of a dynamically adjusted synoptic nowcast/assimilation realization is presented in section 5. Last, section 6 summarizes and concludes.

2. Feature models

For the WNA, which is one of the most intensively studied regions of the World Ocean, most dynamical features are now well known. These include the two jet-scale currents—the GS and the thermohaline DWBC—as well as the subbasin-scale gyres to the north and south of the GS and mesoscale warm and cold core rings. These features are schematized in Fig. 1, which depicts typical synoptic jet structures interacting with mean subbasin-scale (SBS) gyres. The horizontal and vertical distribution of the velocity of the structures are parameterized by analytical or empirical forms obtained from synoptic data. Their geographical location, extent, and realistic range of parameters are obtained from synoptic as well as climatological datasets and synthetical studies; see Table 1.

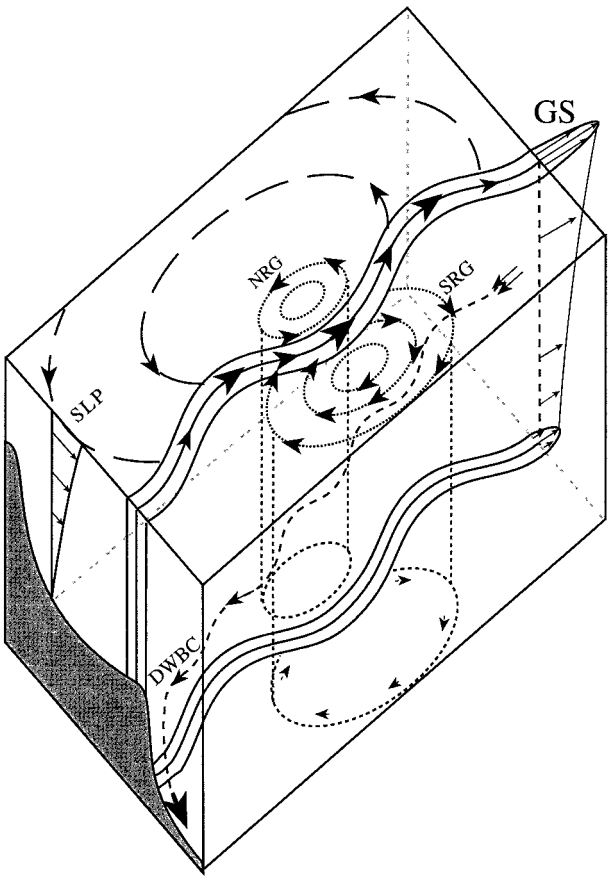

FIG. 1. Schematic of the prevalent features in the Gulf Stream meander and ring (GSMR) region: Gulf Stream (GS), deep western boundary current (DWBC), northern recirculation gyre (NRG), southern recirculation gyre (SRG), and slope water gyre (SLP).

a. Currents

Previous studies have introduced the parameterization of currents as thin jets (e.g., Niiler and Robinson 1967; Robinson et al. 1988; Arango et al. 1992). The purpose here is to provide a parameterization for the velocity structure of any current in any region and to introduce a methodology that provides as realistically as possible profiles consistent with available data. The three-dimensional velocity structures are represented by normalized empirical velocity shears in the vertical and analytical or analytical–empirical horizontal distributions across the jets (see Fig. 2).

The following form can be used as a simple model for the velocity profiles of most currents:

$$u(x, y, z) = \gamma(y)\{[U^T(x) - U^B(x)]\phi(x, z) + U^B(x)\}. \quad (1)$$

Here, $\gamma(y)$ is the nondimensional horizontal velocity dis-

TABLE 1. List of studies used.

Feature	Relevant studies
Gulf Stream (GS)	Niiler and Robinson (1967) Knauss (1969) Richardson and Knauss (1971) Robinson et al. (1974) Halkin and Rossby (1985) Richardson (1985) Hall and Bryden (1985) Watts (1985) Robinson et al. (1988) Spall and Robinson (1990) Hogg (1992)
Deep western boundary current (DWBC)	Pickart and Hogg (1989) Pickart and Watts (1990) Pickart (1992a, 1992b)
Rings	Lai and Richardson (1977) McWilliams and Flierl (1979) Olson (1980) Brown et al. (1986)
Southern recirculation gyre (SRG)	Schmitz (1976) Worthington (1976) Hogg (1992)
Northern recirculation gyre (NRG)	Hogg (1983) Hogg and Stommel (1985) Hogg et al. (1986)
Slope (SLP)	Bisagni and Cornillon (1984) Cornillon et al. (1989) Churchill and Cornillon (1991)

tribution function with a value of unity at the jet axis; $\phi(x, z)$ is the normalized vertical shear profile, with a value of unity at the top and zero at the bottom; x is the dimensional downstream coordinate; y is the dimensional cross-stream coordinate with origin at the location of maximum surface velocity (positive to the left of the flow); and z is the dimensional vertical coordinate (positive upward). Clearly, the second factor (within the curly brackets) on the right side of Eq. (1) contains the baroclinic and barotropic velocity components, $U^T(x)$ being the top velocity and $U^B(x)$ being the bottom velocity at the jet axis at any downstream distance x. Hereafter, top refers to the uppermost location of the feature. Figure 2a shows a typical structure of the jet model and its model parameters, which are further defined in the appendix. Figure 2b shows the Gaussian distribution adapted for the DWBC horizontal velocity profile, and Fig. 2c shows a piecewise continuous analytical fit to the cross-stream nondimensional distribution [$\gamma_{GS}(y)$] for the GS.

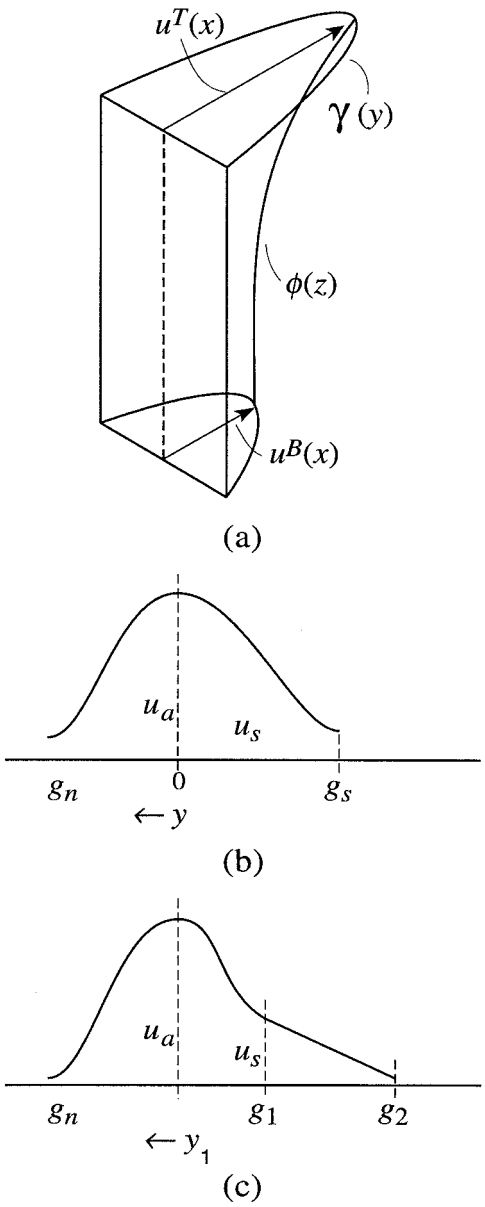

FIG. 2. (a) A typical thin jet model and its parameters; (b) an asymmetric Gaussian velocity distribution; and (c) the piecewise continuous horizontal velocity distribution for the Gulf Stream feature model.

1) THE GULF STREAM

Based on observational studies (Table 1), the three-dimensional velocity distribution for the GS is modeled by a normalized vertical shear profile $\phi_{GS}(x, z)$, a horizontal distribution function $\gamma_{GS}(y)$, and with top and bottom velocities as $U^T_{GS}(x)$ and $U^B_{GS}(x)$. The functional form of $\gamma_{GS}(y)$ is modeled by a piecewise distribution of a combination of linear and exponential functions as given by Eqs. (A1) and (A2) in the appendix, and is shown in Fig. 2c. Explicitly, a Gaussian distribution is chosen on the slope water side, whereas the Sargasso side is represented by two different combinations of linear plus exponential segments so as to maintain continuity of the function and its first derivative. This representation is based on two major dynamical considerations. First, the asymmetric shapes were chosen to reflect the observed asymmetry in the potential vorticity distribution (Leaman et al. 1989) in the upper 200 m,

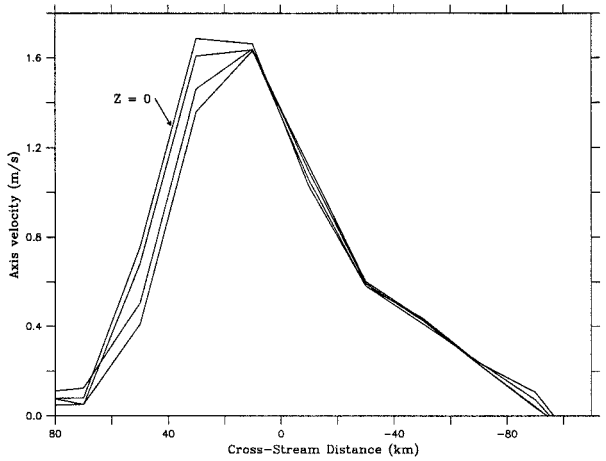

FIG. 3. Pegasus horizontal velocity distribution at different depths in the upper thermocline.

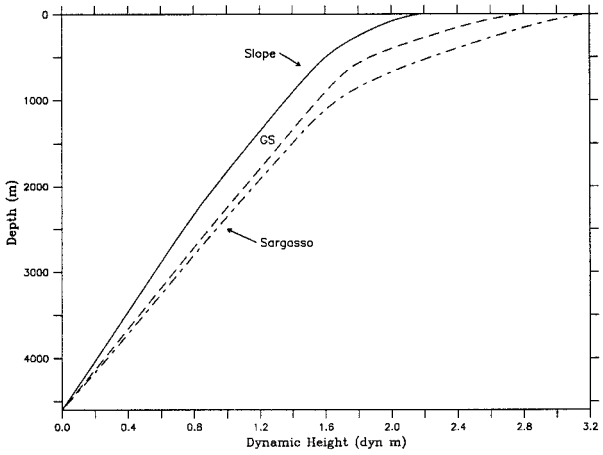

FIG. 4. Averaged profiles of dynamic height anomaly for the slope and Sargasso regions obtained from Levitus climatology and analytical GS structure (derived from the Pegasus synoptic profiles).

which is almost uniform on the offshore side of the stream axis; whereas a pool of positive vorticity dominates the onshore side. Second, the choice of two slightly different linear segments on the Sargasso side was motivated by observations by Halkin and Rossby (1985, hereafter HR). Their stream-coordinate velocity distribution is presented in Fig. 3 for a number of depths in the upper thermocline, which motivated the choice of the piecewise analytical expression given by Eq. (A1).

To evaluate the free parameters of the adopted analytical form of $\gamma_{GS}(y)$, both climatological and synoptic hydrographic information were utilized. First, the slope and Sargasso climatological dynamic height profiles (ΔD_{SLP}, ΔD_{SAR}) are derived relative to the mean bottom from the Levitus (1982) atlas. They are computed from the average temperature–salinity profile over the regions bounded by the 75° and 50°W longitudes and to the north and to the south of the climatological stream. These average profiles are shown in Fig. 4 along with the synoptic dynamic height profile at the stream axis (ΔD_{GS}) obtained from the Pegasus hydrographic data (HR). The integral of the velocity distribution is then constrained to match the difference of the Sargasso/slope climatological dynamic height profile at the edge of the stream and the synoptic Pegasus profile at the stream axis. Mathematically, these constraints are

$$\int_0^{g_n} u_{GS}(x, y, z)\, dy = (\Delta D_{SLP} - \Delta D_{GS})\frac{10}{f} \qquad (2a)$$

$$\int_{-g_2}^{0} u_{GS}(x, y, z)\, dy = (\Delta D_{GS} - \Delta D_{SAR})\frac{10}{f}. \qquad (2b)$$

Thus, the three vertical profiles of Sargasso, slope, and the GS dynamic height determine the choice of the free parameters of the GS horizontal velocity profile structure at Cape Hatteras.

Using such an integral constraint methodology, once we chose the two speeds, one at the axis (u_a = 175 cm s^{-1}) and the other at $y = -g_1$ ($u_s = 0.37u_a$) on the Sargasso side (see Fig. 2c), the free parameters obtained are g_1 = 40 km, g_2 = 110 km, and g_n = 45 km. A very good fit is obtained when the value of *e*-folding lengths, l_1 and l_2, are set to 5 km. Note, however, that we are free to choose a different axis velocity (u_a), within reasonable limits of observations. The central parameter values and their observational ranges for the GS and all other features are listed in Table 2.

The average synoptic velocity distribution of the GS at 73°W derived by HR is shown in Fig. 5a. Note that the offshore tilt of the GS maximum velocity axis, evident in both Figs. 3 and 5a, is varied linearly from zero at the surface to a maximum value of 30 km at 800 m in the feature model representation. The vertical shear profile ϕ_{GS}(73°W, *z*) is determined by normalizing the axis velocity with respect to its value at the surface from the Pegasus data. Using this normalized vertical structure with a surface axis speed of 175 cm s^{-1}, and the width and tilt parameters discussed above, the feature model velocity distribution for the GS is obtained using Eq. (1) and is shown in Fig. 5b. This representation is not only the best fit to the synoptic information of the GS as known today but also agrees with the dynamic heights obtained from the climatological slope and Sargasso *T–S* profiles.

In reality, the GS transport increases from about 70 Sv near Cape Hatteras to about 150 Sv at 60°W and then decreases farther downstream. Such a change in transport is due to changes in both barotropic and baroclinic components of the flow. The baroclinic change can be modeled in part by introducing a change in the normalized shear profile $\phi_{GS}(x, z)$ with longitude, which is discussed in section 3. These longitudinally dependent shear profiles at Cape Hatteras and at 60°W are shown in Fig. 6.

TABLE 2. Central set of multiscale circulation model parameters.

Parameter	Value	Range	Comment
g_n	45 km		GS width in the slope side
g_1	40 km		G1 width in the Sargasso side
g_2	110 km		G2 width in the Sargasso side
U_H^T	1.30 m s^{-1}	1.0–1.5 m s^{-1}	GS top velocity at Cape Hatteras
U_H^B	0.0 m s^{-1}	0.0–0.5 m s^{-1}	GS bottom velocity at Cape Hatteras
Z_{lnm}	4600 m		Level of no motion
S_{tilt}	30 km	15–30 km	GS axis tilt
Z_{tilt}	800 m	700–1000 m	Depth of maximum tilt
g_W^n	50 km		DWBC northern width
g_W^s	50 km		DWBC southern width
Z_{DWBC}^T	800 m		DWBC shallowest depth
Z_{DWBC}^B	4600 m		DWBC bottom depth
U_{DWBC}^T	0.0 cm s^{-1}		DWBC velocity at Z_{DWBC}^T
U_{DWBC}^B	20 cm s^{-1}	15–40 cm s^{-1}	DWBC velocity at Z_{DWBC}^B
$C_{\text{SRG}}^{\text{lon}}$	60°W		Longitude for SRG center
$C_{\text{SRG}}^{\text{lat}}$	38°N		Latitude for SRG center
A_{SRG}	700 km		SRG major axis
B_{SRG}	500 km		SRG minor axis
U_{SRG}^T	7 cm s^{-1}	6–10 cm s^{-1}	SRG velocity at Z_{SRG}^T
U_{SRG}^B	2 cm s^{-1}	2–5 cm s^{-1}	SRG velocity at Z_{SRG}^B
$C_{\text{NRG}}^{\text{lon}}$	56°W		Longitude for NRG center
$C_{\text{NRG}}^{\text{lat}}$	42.4°N		Latitude for NRG center
A_{NRG}	500 km		NRG major axis
B_{NRG}	100 km		NRG minor axis
U_{NRG}	3.5 cm s^{-1}	3–5 cm s^{-1}	NRG barotropic velocity
$C_{\text{SLP}}^{\text{lon}}$	62°W		Longitude for SLP center
$C_{\text{SLP}}^{\text{lat}}$	40°N		Latitude for SLP center
A_{SLP}	1800 km		SLP major axis
B_{SLP}	400 km		SLP minor axis
U_{SLP}	3 cm s^{-1}	3–6 cm s^{-1}	SLP top velocity

2) THE DEEP WESTERN BOUNDARY CURRENT

The DWBC was first postulated by Stommel (1957) and later verified by investigators such as Swallow and Worthington (1961) and Volkman (1962). Recent observations by Hogg (1983) and Hogg et al. (1986) have shed more light on this deep boundary current. The structure and hydrography of the current have been extensively studied by Pickart and Hogg (1989), Pickart and Watts (1990), and Pickart (1992a,b). The DWBC enters the GSMR region at about 47°W and follows the 3400 ± 200 m bathymetric contour from the Grand Banks of Newfoundland to just south of Cape Hatteras. The path of this deep current is shown in Fig. 7a, with the topography of the region. South of Cape Hatteras, it passes beneath the GS, and at the Blake–Bahama rise it flows along the 4200 ± 200 m isobath.

The along-stream velocity component for the DWBC may be given in accordance with Eq. (1). Here, its nondimensional horizontal velocity structure $\gamma_w(y)$ is modeled as a symmetric Gaussian distribution over its width g_w; that is, $\gamma_w(y) = e^{-y^2/g^2}w$. The top (at 800 m) and bottom axis velocities and the vertical shear profile for this thermohaline jet are assumed independent of the downstream distance (x) for this simple model. This zero-order representation of the DWBC can be significantly improved once a better observational understanding of the downstream variation/interaction of the DWBC with surrounding gyres is established.

A schematic representation of the adopted DWBC velocity profile is shown in Fig. 7b. The nondimensional vertical shear profile $\phi_w(z)$ for the DWBC is shown in Fig. 6 and is represented by

$$\phi_w(z) = \frac{\Delta\psi_w^*(z)}{\dfrac{1}{H}\displaystyle\int_0^H \Delta\psi_w^*(z)\, dz}, \tag{3}$$

where $\Delta\psi_w^*(z) = (g/f_o)(\Delta\overline{D}_w)$ and $\Delta\overline{D}_w$ is the dynamic height difference across the undercurrent evaluated from a melding of climatological data (T–S relationship) and recent observational studies by Pickart and Watts (1990) and Pickart (1992a). Following the observational studies listed in Table 1, we chose a bottom velocity of 20 cm s^{-1} for a 100-km-wide current with a transport of 30 Sv as the central set of DWBC parameters.

3) THE INTERACTION BETWEEN THE GS AND THE DWBC

A major consideration in the development was modeling the crossover between the two currents. Based on observations, Hogg and Stommel (1985) proposed a two-layer dynamical model in which the DWBC would change its path following the 3400-m isobath to the 4200-m isobath while sliding under the 800-m-deep thermocline of the GS at Cape Hatteras in order to conserve its potential vorticity. Observational analysis in

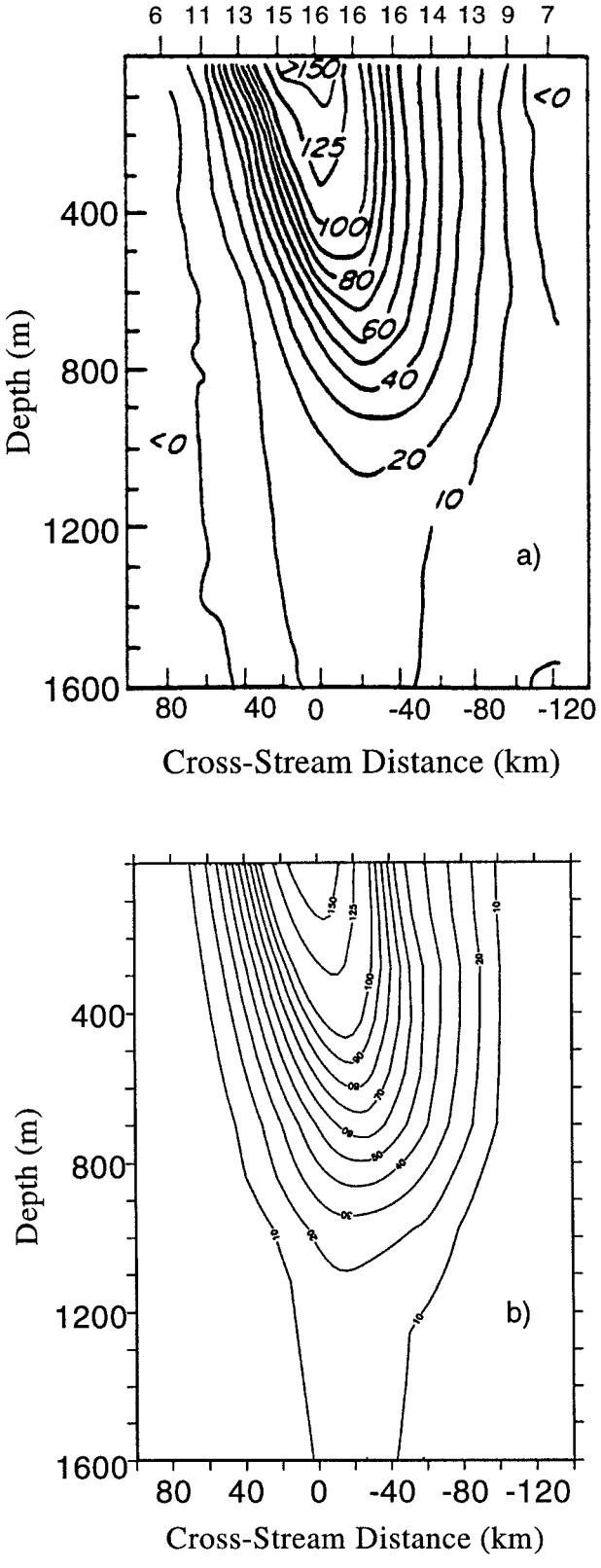

FIG. 5. Gulf Stream velocity sections (a) from Pegasus average synoptic profile and (b) from multiscale feature model.

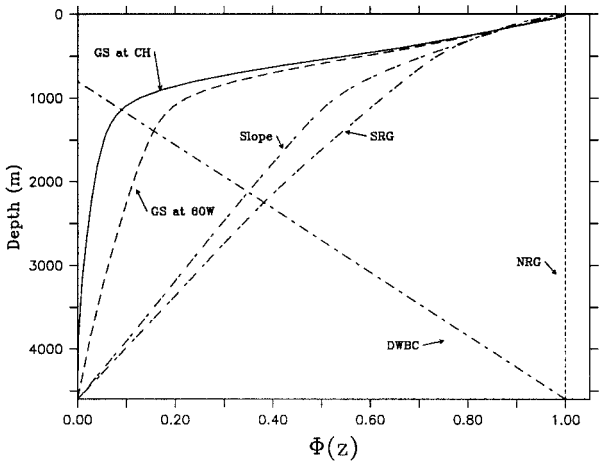

FIG. 6. Nondimensional vertical shear profiles, $\phi(x, z)$ for the Gulf Stream at Cape Hatteras and 60°W, DWBC, NRG, SRG, and SLP.

support of this mechanism was found by Pickart (1992b); however, more recent observations (Pickart and Smethie 1993) showed multiple pathways at different depths during the crossover. In each synoptic realization represented by our linked feature models, the

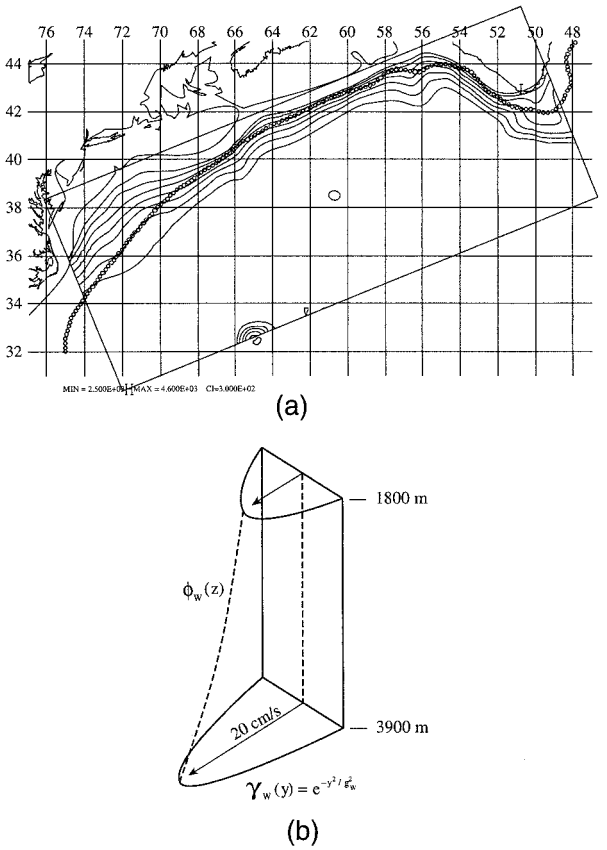

FIG. 7. The deep western boundary current: (a) Its mean axis on the underlying topography of the region and (b) its velocity structure in the deep (1800–2700 m) waters.

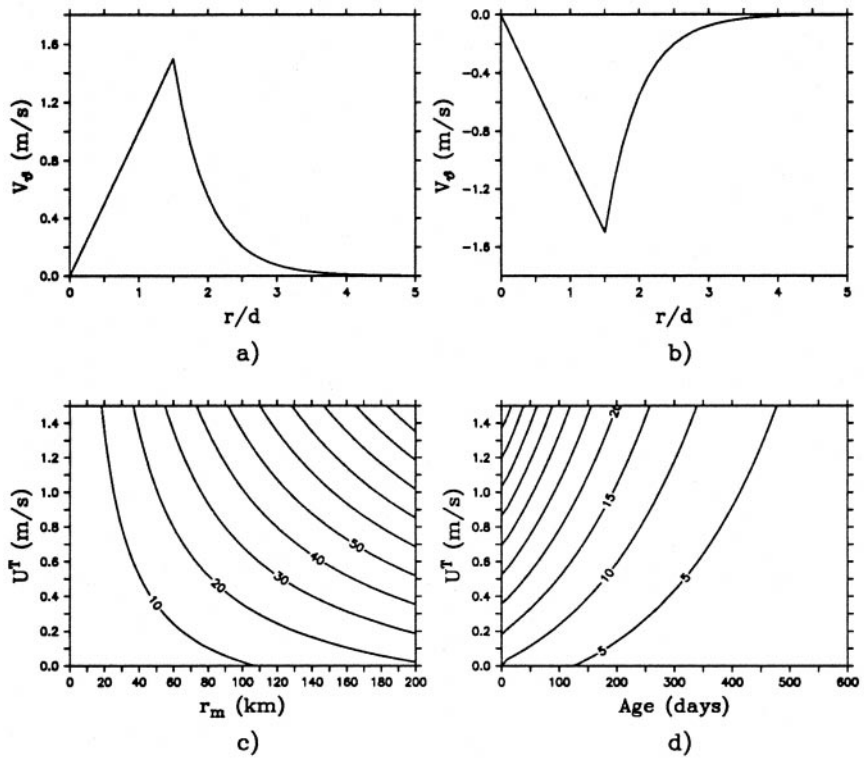

FIG. 8. The nondimensional horizontal velocity distribution for (a) cold core and (b) warm core rings. Transport variation for a typical synoptic ring as a function of (c) maximum speed at the surface and nondimensional axial distance r/d and of (d) U^T and ring age.

mean path of the undercurrent is altered in each application according to the synoptic configuration of the GS, before, while, and after it crosses the stream, so that the potential vorticity is conserved at the crossover region according to the simple two-layer model of Hogg and Stommel (1985). Explicitly, the 3400-m isobath is followed for the DWBC up to the synoptic onshore edge of the stream, and the 4200-m isobath is followed southwest of the offshore edge of the stream, with a smooth subjective interpolation under the stream at the initialization. However, when the quasigeostrophically adjusted feature model fields are integrated via the dynamical numerical model, potential vorticity is expected to be conserved in detail in the ensuing integration. Such numerical integrations show that the DWBC splits up in several segments (see Figs. 13b,c) in the crossover region during the initial adjustment stages of model simulations in agreement with Pickart and Smethie (1993).

b. The rings

Several observational studies (Table 1) have been used to model the structure of the rings generated by the breaking meanders of the GS. The rings are assumed to be circular or elliptical and modeled, in the horizontal, with a linear velocity profile out to a maximum value v_m followed by an exponential decay, as shown in Figs. 8a and 8b for a cold (cyclonic) and warm (anticyclonic) core ring, respectively. In the vertical, the velocity shear profile is obtained from the Pegasus data for the synoptic GS axis profile. In addition, an attenuation effect due to the ring's age is incorporated.

For a circular ring, the azimuthal velocity component v_θ is taken as

$$v_\theta(r, z) = \begin{cases} \dfrac{r}{r_0} v_m \phi_R(z) e^{-t_a/t_0}, & \text{for } 0 \le r \le r_0 \\ v_m e^{\alpha(1-r/r_0)} \phi_R(z) e^{-t_a/t_0}, & \text{for } r > r_0, \end{cases} \tag{4}$$

where v_m is the maximum azimuthal velocity in the ring, r_0 is the radius at which maximum velocity is reached, $\phi_R(z)$ is the vertical structure with baroclinic and barotropic components, α is a positive constant, t_a is the time since birth for a ring that has not been interacting with the GS, and t_0 is the age attenuation scale. Note that the bimodality of t_0 (Brown et al. 1986) is neglected in this version of the ring feature model. The analytical equations for the elliptical rings are similar to those of the SBS features described in the next section.

The dependency of the ring parameters on the axial volume transport is presented in Figs. 8c and 8d for a cyclonic ring. The tunable parameters (independent

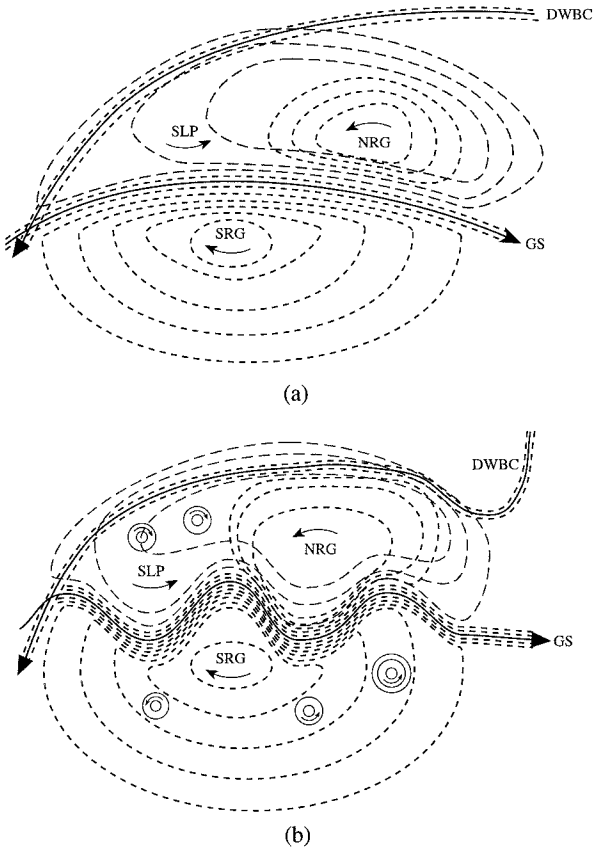

FIG. 9. Schematics of the recirculation gyres within the Gulf Stream system: (a) The mean state and (b) typical synoptic state with deformed ellipses.

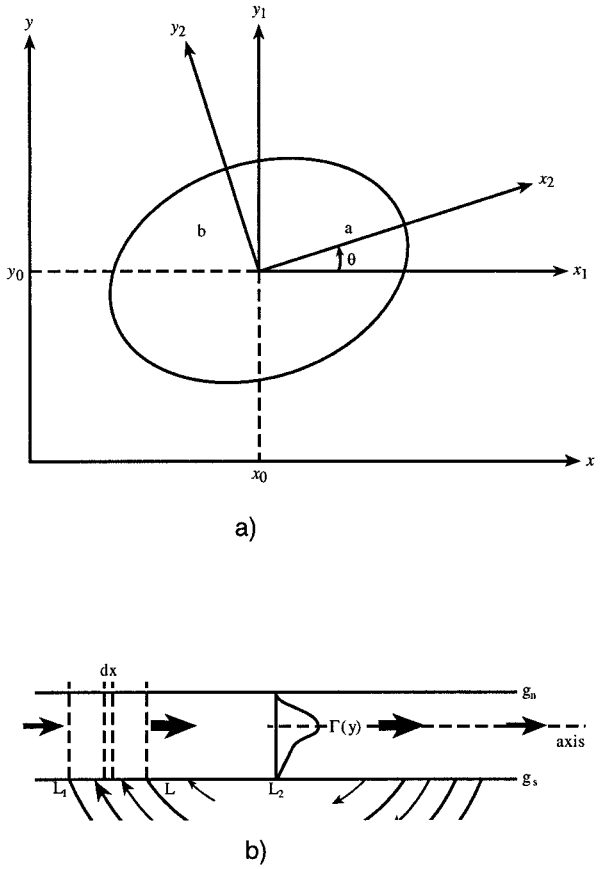

FIG. 10. (a) Schematic of an elliptic gyre. (b) A synoptic perspective of the kinematic synthesis.

variables) are maximum azimuthal velocity v_m, bottom velocity v_b, maximum radius r_m, and age t_a. Here, the radius of maximum velocity is taken as $r_0 = 0.6r_m$. Following Olson (1980), the value of α is chosen as 3. Generally, an *e*-folding attenuation scale of 200 days [closer to long-life rings according to Brown et al. (1986)] is assumed that agrees with the values given by Flierl (1977) and McWilliams and Flierl (1979). For a typical cold core ring (CCR) of a 100-km radius and maximum azimuthal velocity of 150 cm s^{-1}, the axial volume transport is about 60 Sv at birth ($t_a = 0$). Its axial transports spins down to 20 Sv in about 6 months.

c. The subbasin-scale gyres

The GSMR region schematized in Fig. 1 contains three subbasin-scale gyres, which are shown in Fig. 9 in their mean and synoptic conceptual states. Following various observational and synthetical studies listed in Table 1, these gyres are modeled with elliptic or partially elliptic functions in their mean state.

1) AN ELLIPTIC GYRE FEATURE MODEL

The synopsis of an elliptic gyre is shown in Fig. 10a. The elliptic streamline is rotated by an angle θ with respect to the latitudinal–longitudinal grid X_1, Y_1 at the center of the gyre (x_0, y_0). The horizontal velocity components at any grid point (x_p, y_p) are given by

$$u = u_p \cos\theta - v_p \sin\theta, \tag{5a}$$

$$v = v_p \cos\theta - u_p \sin\theta, \tag{5b}$$

where

$$u_p(r, z) = \gamma(r)[(U^T - U^B)\phi(z) + U^B] \tag{5c}$$

and

$$v_p(r, z) = \gamma(r)[(V^T - V^B)\phi(z) + V^B]. \tag{5d}$$

Here, U^T is the zonal component of the maximum top (surface) tangential velocity $V^T_{\max}$ of the ellipse located at a distance r ($r^2 = a^2 \cos^2\alpha + b^2 \sin^2\alpha$) from its center; a and b are the major and minor axes of the ellipse, $r_p^2 = x_p^2 + y_p^2$. This representation was first used by S. Glenn (1992, personal communication). The phase α of a particular orbit connects the two components of the tangential velocity through the angular frequency ($\omega = V^T_{\max}/a$) such that, $U^T = \omega a \sin\alpha$ and the meridional component, $V^T = \omega b \cos\alpha$. Note that the sign of ω would determine the sense of the direction: cyclonic (positive) and anticyclonic (negative). Here $\gamma(r)$ is the

nondimensional shape function for the horizontal velocity distribution in a particular gyre, and $\phi(z)$ is the nondimensional vertical shear profile for the gyre that is derived by melding climatology with observational synoptic datasets described below.

2) The southern recirculation gyre

The region to the south of the GS is believed to be a region of recirculation driven by eddies. The first description of this gyre was given by Worthington (1976), followed by several other investigators (see Table 1). In this multiscale circulation model, this gyre is implemented as an anticyclonic elliptical feature that feeds into the GS as well as feeds itself from the stream.

The azimuthal velocity at any point within this gyre is given by Eq. (1), where the parameters on the right-hand side relate to those of the SRG. The nondimensional horizontal velocity distribution function $\gamma_{\mathrm{SRG}}(r)$ is represented by Eq. (A3). The vertical shear profile $\phi_{\mathrm{SRG}}(z)$ shown in Fig. 6 is evaluated from the climatological Sargasso dynamic height (Fig. 4) according to the relationship given by Eq. (A4). The center of the model SRG is located at 38°N, 60°W, with major and minor axes at 700 and 400 km, respectively. Typical observational range (Schmitz 1976; Richardson 1985) for the top and bottom velocities of the SRG are around 6–10 cm s^{-1} and 0–5 cm s^{-1}, respectively.

3) The northern recirculation gyre

In contrast to Worthington's (1976) picture of an anticyclonic gyre to the north of the GS, recent observational analyses (Hogg 1983; Hogg et al. 1986) indicate a cyclonic barotropic gyre called the northern recirculation gyre (NRG). This is shown schematically in Fig. 9 as a bounded recirculation between the GS and the DWBC. As in the model by Hogg and Stommel (1985), the horizontal velocity increases linearly to a maximum at the elliptical boundary and decreases exponentially beyond the gyre. The exact form of $\gamma_{\mathrm{NRG}}(r)$ is given by Eq. (A5). Since there is no vertical shear for this barotropic gyre, $\phi_{\mathrm{NRG}}(z) = 1$ (see Fig. 6).

The NRG, as implemented, is centered at 42.4°N, 56°W, with a meridional extent of 100 km and a zonal extent of 500 km. The total transport carried by the NRG in its mean adaptation (with a maximum velocity of 3.5 cm s^{-1}) is 40 Sv, including 15 Sv of flow recirculating with the stream. A realistic range for the maximum velocity for the NRG is 3–6 cm s^{-1}.

4) The slope water gyre

The region to the north of the GS, called the slope water, is believed to be a region of slow westward flow primarily inhabited by the warm core rings detached from the GS (Churchill and Cornillon 1989; see Table 1). Since this region is bounded by the stream to its south and by coastal boundaries to its north, it is reasonable to assume that it is a broad cyclonic gyre, slowly coming westward to join the GS and returning eastward with the stream (Bane et al. 1988). The bottom velocity of this gyre is set to zero, so that the deep circulation to the north of the stream primarily comprises the DWBC and the NRG.

The azimuthal velocity at any point within this gyre is given by Eq. (1), where $\gamma_{\mathrm{SLP}}(r)$ is represented by Eq. (A6), and $\phi_{\mathrm{SLP}}(z)$ (Fig. 6) is evaluated from the climatological slope water dynamic height (Fig. 4) according to Eq. (A7). The center of this 1800 km × 500 km wide gyre is located at 42°N, 62°W. Note that this gyre overlaps with the NRG to a certain extent primarily in the upper thermocline regime, as shown in Fig. 9. Typical observational values (Bisagni and Cornillon 1984) for the top velocity in the SLP are between 5 and 10 cm s^{-1}.

d. Synoptic deformation of the mean state

The mean state for this circulation system is taken to be the average synoptic current structures located at their mean axes and interacting with the mean gyres, as shown in Fig. 9a. In order for any gyre feature to be represented in a particular synoptic state, the mean-state boundary of the feature is distorted to conform to the synoptically available region for the feature (see Fig. 9b). This is achieved within the constraint of mass conservation for the SBS gyre itself. Specifically, the mass flow through any longitudinal section of the mean-state ellipse is conserved in the synoptic state by appropriately altering the velocity distribution throughout the modified zonal extent of the gyre. The net effect is either a smaller (with stronger velocity distribution than in the mean state) recirculation than the climatological one or a larger (with reduced velocity distribution) gyre, but always with fixed mass transport. Observational evidence of such a mass conserving scenario for the NRG–GS interaction was found by Bane et al. (1988). They found that the mean monthly shelfbreak currents were strongest when the GS was close (150 km) to the shelf edge, whereas those same currents were almost negligible when the stream was about 300 km away from the shelf edge.

While the background circulation is represented in the synoptic configuration by such deformation of the mean state; in reality the ocean is dominated by mesoscale and submesoscale activity synoptically. Mesoscale features like the warm and cold core rings are embedded in the deformed background circulation for a typical synoptic realization (see Fig. 9b). Knowledge of open-ocean mesoscale eddies is added when available either by simple feature models or as a direct gridded data stream (e.g., satellite altimetry). Submesoscale structures in the Sargasso Sea and to the north of the stream like open-ocean eddies, shingles, and intrusions are not included in this study. In the absence of addi-

tional synoptic datasets, the deformed mean state gyres will adjust with the synoptic stream and rings configuration. Initial dynamical balance is obtained via quasigeostrophic dynamics discussed in section 5b, and once the dynamical simulation is in progress, wind and thermal forcing may produce such meso- or submesoscale structures that should be in dynamical balance with the surrounding multiscale environment.

3. A synthesized circulation model

The regional circulation for the GSMR region consists of the multiscale circulation structures described in the previous section. Now that the feature model representations of these structures have been constructed, a kinematic synthesis of these features into a three-dimensional velocity distribution is the next step. Such a multiscale circulation model synthesizes information on several scales including mesoscale, subbasin scale, and large scale. The major dynamical structure in the GSMR region is the GS, which is large scale downstream, jet scale cross stream, mesoscale in its meandering, and subbasin scale in its transport increase and decrease as it interacts with the subbasin-scale gyres to the south and to the north. The kinematical interconnection of the features through GS transport increase and decrease with mass conservation constitutes a new circulation model for the region. This kinematical interconnection is achieved through constrained interaction between features. The barotropic and baroclinic mass exchange between any gyre and the stream is shown to vary proportionately with the ratio of their respective interaction scales.

a. Kinematics of multiscale interaction

As the stream flows downstream, it is joined by the SRG, which is anticyclonic and thus adds transport by adding both baroclinic shear flow and barotropic velocity (bottom) (see Fig. 10b). Due to continuity, the total mass flux coming normal to the southern edge of the GS between L_1 and L would increase the transport of the stream over this length. Clearly, the baroclinic flux "input" I_{bc} from the SRG into the stream from L_1 to L is given by

$$I_{bc} = \int_{-H}^{0}\int_{L_1}^{L} \gamma_{SRG}(r)(U^T_{SRG} - U^B_{SRG})\phi_{SRG}(z)\, dz\, dr$$
$$= \Gamma_{SRG}\Phi_{SRG}(U^T_{SRG} - U^B_{SRG}), \quad (6)$$

where

$$\Gamma_{SRG} = \int_{L_1}^{L} \gamma_{SRG}(r)\, dr$$

and

$$\Phi_{SRG} = \int_{-H}^{0} \phi_{SRG}(z)\, dz.$$

Let us assume that the baroclinic transport increase in this segment of the stream is only due to above baroclinic flux injection from the SRG. And, it is also reasonable to assume that the infused Sargasso water [with vertical shear $\phi_{SRG}(Z)$] does not affect the horizontal velocity distribution [$\gamma_{GS}(y)$] of the stream. The effective change in the stream can then be formally represented by a small but significant increase in its axis velocity at the top (U_i^T) and at the bottom (U_i^B) in an integral sense. The increase in baroclinic transport T_{bc} in the stream over the same length can then be written as follows:

$$T_{bc} = \int_{-H}^{0}\int_{-g_2}^{g_n} \gamma_{GS}(y)[U_i^T - U_i^B]\phi_{SRG}(z)\, dy\, dz$$
$$= \Gamma_{GS}[U_i^T - U_i^B]\Phi_{SRG}, \quad (7)$$

where

$$\Gamma_{GS} = \int_{-g_2}^{g_n} \gamma_{GS}(y)\, dy.$$

Thus, equating these baroclinic flow components, that is, $I_{bc} = T_{bc}$, one gets

$$\frac{U^T_{SRG} - U^B_{SRG}}{U_i^T - U_i^B} = \frac{\Gamma_{GS}}{\Gamma_{SRG}}. \quad (8)$$

Similarly, equating their barotropic counterparts, that is, $\Gamma_{SRG}HU^B_{SRG} = \Gamma_{GS}HU_i^B$, and using this with Eq. (8), we get the following interaction relationship between these two features:

$$\frac{U_i^T}{U^T_{SRG}} = \frac{U_i^B}{U^B_{SRG}} = \frac{\Gamma_{SRG}}{\Gamma_{GS}}. \quad (9)$$

We now redefine this interaction length scale as the integral over the region of interaction between the GS and the SRG, that is, $\Gamma_{SRG} = \int_{L_1}^{L_2} \gamma_{SRG}(r)\, dr$. Note that γ_{SRG} is nondimensional, and so Γ_{SRG} represents the dimensional interaction length scale. Thus, the velocity influx at the top and bottom from the SRG to the stream is proportional to the ratio of its interaction length to that of the stream. Similarly, the increase in top and bottom velocities of the GS from the other features would be proportional to the ratios of their respective interaction length scales to that of the stream, which can be added to get the transport of the GS at any location.

b. Characteristics of the interaction parameters— $\boldsymbol{\Gamma}$ *and* $\boldsymbol{\Phi}$

As shown above, the interaction between different features is dependent on their model parameters, namely, the top (surface) and bottom velocities, the vertical shear profile integral (Φ), and their respective size and locations. A formal problem of optimizing the parameters, sizes, and locations would be very demanding.

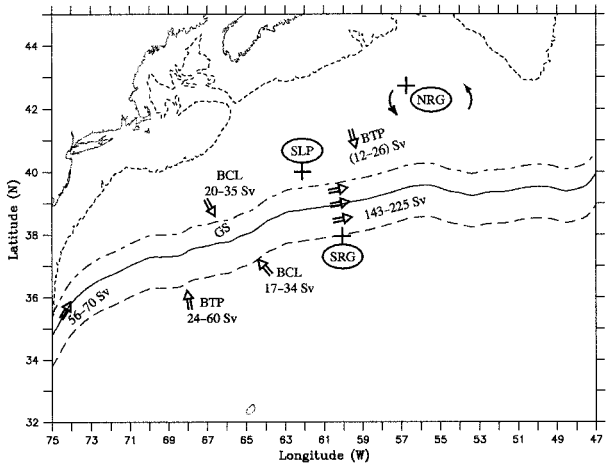

FIG. 11. The transport cartoon as derived from the circulation model analysis. The centers of the SBS gyres are marked as a plus sign. The ranges of transport influx from various gyres into the GS are depicted as part barotropic and part baroclinic.

We are, however, knowledgeable about the mean sizes and locations of the various features, and as a reasonable choice of central values, we fix the sizes and locations of the three different gyres based on observational studies. Their locations and extents are listed in Table 2 and shown in Fig. 11.

The interaction length scales (Γ) are dependent on the horizontal velocity distribution and the interaction extents of different features. These are evaluated for the mean positions of the SBS features and are listed in Table 3 as a factor of Γ_{GS}. For the GS $L_1 = -g_2$, and $L_2 = g_n$; whereas for the SRG, SLP, and NRG, they are dependent on the geographical extent of interaction between the individual feature and the stream. Note that the interaction length ratio for the SLP is the maximum since it has the largest interaction extent with the stream. The NRG, which is of limited size, has the least interaction with the GS. The southern gyre, although of medium interaction length, plays an effective role in adding both baroclinic and barotropic mass to the GS system. The depth integral Φ of the vertical shear profile for individual features gives a measure of their effective baroclinic depth and is presented in Table 3 as a factor of the mean depth (4600 m) of the region.

c. The synthesis

As shown in the preceding two sections, the essential kinematical mechanism by which the regional background features interact with the GS can be comprehended by an increase in the axial velocity of the GS at each location downstream of Cape Hatteras. We are now in a position to determine this downstream variation of the velocity structure of the GS in terms of the SBS feature parameters. In the following, the subscript ''H'' denotes the value of the parameters at Cape Hatteras. As the SBS gyres inject mass into the stream, this structure modifies longitudinally up to 60°W and beyond through injection and extraction of mass.

TABLE 3. Multiscale integral parameters: $\overline{\Gamma}_f = \int_L \Gamma(r)\, dr$, $\Phi_f = \int_H \phi(z)\, dz$, $\overline{\Gamma}_{GS} = 74.20$ km, and $H = 4600$ m.

Feature	Interaction scale ratio ($\overline{\Gamma}_f/\overline{\Gamma}_{GS}$)	Integral depth factor ($\overline{\Phi}_f/H$)
GS at Hatteras	1.0	0.16
GS at 60°W	1.0	0.20
DWBC	1.01	0.41
NRG	1.25	1.0
Slope	5.23	0.39
SRG	3.52	0.36

So, the velocity at 60°W for the GS at any depth can be written as

$$U_{GS}(60W, z) = \left\{[(U_H^T - U_H^B)\phi_H(z) + U_H^B] + \frac{\Gamma_{SLP}}{\Gamma_{GS}} U_{SLP}^T \phi_{SLP}(z) + \frac{\Gamma_{NRG}}{\Gamma_{GS}} U_{NRG} + \frac{\Gamma_{SRG}}{\Gamma_{GS}}[(U_{SRG}^T - U_{SRG}^B)\phi_{SRG}(z) + U_{SRG}^B]\right\}\gamma_{GS}(y). \quad (10)$$

Also, from (1),

$$U_{GS}(60W, z) = [(U_{60W}^T - U_{60W}^B)\phi_{60W}(z) + U_{60W}^B]\gamma_{GS}(y). \quad (11)$$

For all features, $\phi(x, z = 0) = \gamma(y = 0) = 1$. Equating (10) and (11) results in

$$\phi_{GS}(60W, z)(U_{60W}^T - U_{60W}^B) = (U_H^T - U_H^B)\phi_H(z) + \frac{\Gamma_{SLP}}{\Gamma_{GS}} U_{SLP}^T \phi_{SLP}(z) + \frac{\Gamma_{SRG}}{\Gamma_{GS}}[(U_{SRG}^T - U_{SRG}^B)\phi_{SRG}(z)]. \quad (12)$$

So, the vertical shear profile at 60°W, $\phi_{GS}(60W, z)$ is determined to account for appropriate baroclinic and barotropic changes by the inclusion of different SBS features downstream (see Fig. 6). Note that the generalized form of the above formulation [Eqs. (10)–(12)] facilitates the numerical implementation of a variable transport stream in contrast to the previously well-known constant transport stream feature models (Spall and Robinson 1990; Glenn and Robinson 1995).

Once the velocity fields for all of the interacting features are melded together in the model domain, the above implementation of the GS system helps minimize the discontinuity at the gyre/front boundaries that would have appeared otherwise. The melding procedure and further adjustment to the stratification of the region via a Poisson solver are described in section 5.

d. Final parameters and constraints of the synthesis

Following our discussion above on determining contributions from different features into the stream, the top and bottom velocity at 60°W can be written as

$$U^T_{60W} = U^T_H + \frac{\Gamma_{SRG}}{\Gamma_{GS}} U^T_{SRG} + \frac{\Gamma_{SLP}}{\Gamma_{GS}} U^T_{SLP} + \frac{\Gamma_{NRG}}{\Gamma_{GS}} U_{NRG} \tag{13}$$

and

$$U^B_{60W} = U^B_H + \frac{\Gamma_{SRG}}{\Gamma_{GS}} U^B_{SRG} + \frac{\Gamma_{NRG}}{\Gamma_{GS}} U_{NRG}. \tag{14}$$

Considering the facts that the NRG is barotropic and that $U^B_{SLP} = 0$, the final six free parameters in this circulation model are U^T_H, U^B_H for the GS at Cape Hatteras; U^T_{SRG}, U^B_{SRG} for the SRG; U^T_{SLP} for the SLP; and U_{NRG} for the NRG.

The maximum transport of the GS at 60°W can also be determined in terms of these free parameters by adding contributions from different sources as follows:

$$T_{60W} = T_H + \Gamma_{SRG}\{\Phi_{SRG}(U^T_{SRG} - U^B_{SRG}) + HU^B_{SRG}\} + \Gamma_{SLP}\Phi_{SLP}U^T_{SLP} + \Gamma_{NRG}HU_{NRG}. \tag{15}$$

This is the transport constraint that the choices of free parameters must satisfy. Note that for the same amount of increase of transport ($T_{60W} - T_H$), one can choose the parameters in such a manner so that most of the increase is due to baroclinic sources, only barotropic sources, or a controlled choice of both effects.

Using a realistic range around the typical observational values of top and bottom velocities for the individual features, and utilizing the interaction length scales and effective baroclinic depths, the transports of the individual multiscale features are evaluated and presented in Fig. 12. Note that the increase in the GS transport at 60°W (Fig. 12b) relative to that at Cape Hatteras (Fig. 12a) for the same pair of U^T and U^B values is due to the downstream change of its shear profile. Figure 12c shows the linear dependence of the DWBC transport on its bottom velocity resulting from the fixed depth integrated value (Φ_W) and a zero top velocity at 800 m. Similar linear dependence is obtained for the NRG with respect to its barotropic maximum velocity (Fig. 12d). Finally, the last two panels (Figs. 12e,f) present the transports of the recirculating SLP and SRG, as functions of their top and bottom velocities.

4. The synoptic-stream climatology

Multiscale feature models described in section 2, and their kinematic synthesis as developed in section 3, represent a powerful approach to describe any regional circulation. In this section, we use the kinematic approach to develop a regional circulation model based on climatological gyres and the climatology of the synoptic GS structure to yield a ''synoptic-stream climatology'' for the GSMR region. The observed parameter ranges for the multiscale features will then define a realistic range of possible transport bounds for the GS system. This also provides a reasonable estimate of transport fluxes into the GS system. Finally, we present the actual realization of this particular climatology that will be used for calibrating and validating a primitive equation model in Part II (Robinson and Gangopadhyay 1997; hereafter RG).

a. Parameters of the synoptic-stream climatology

Based on observational analyses (Table 1) we chose 60°W, as the location for the maximum transport in the stream, which coincides with the center of the baroclinic SRG (Fig. 11). The SLP is centered at 62°W and thus feeds itself from the stream between 62° and 60°W. The NRG is centered at 56°W, thus a part of it (61°–60°W) would only feed into the stream; the rest of this gyre (between 60° and 57°W) balances the outflow to the SRG to maintain the constant transport stream between 60° and 57°W. To the east of 57°W we allow the stream to gradually reduce its transport to its value at Hatteras to conserve mass across the domain and to be consistent with feeding the recirculating gyres.

The central set of values listed in Table 2 is chosen for the appropriate parameters of the synoptic-stream climatology. For a value of $U^T_{GS} = 130$ cm s^{-1}, and $U^B_{GS} = 0$, the stream carries a transport of 70 Sv at Cape Hatteras from Fig. 12a. The influx from NRG with a $U_{NRG} = 3.5$ cm s^{-1} is 14.5 Sv. For $U^B_{SLP} = 0$ and $U^T_{SLP} = 3.0$ cm s^{-1}, the SLP carries a recirculating transport of 22 Sv. The central choice for SRG ($U^T_{SRG} = 7.0$ cm s^{-1} and $U^B_{SRG} = 2.0$ cm s^{-1}) yields a SRG influx of 46 Sv. The stream transport at 60°W is thus determined by Eq. (15) as 152.5 Sv. On the other hand, if one uses Eqs. (13) and (14), the top and bottom velocities of the stream at 60°W are determined as 175 and 11.4 cm s^{-1}, respectively. Using these values the transport of the stream at 60°W is obtained as 153 Sv from Fig. 12b. Thus, the transport constraints defined in section 3d are satisfied for the chosen set of parameters of the synoptic-stream climatology.

b. Transport bounds of the GS system

In this circulation model, the GS carries a primarily baroclinic transport in the range of 56–70 Sv at Cape Hatteras (see Fig. 11). As it flows downstream, the recirculating SLP adds primarily baroclinic transport of about 20–35 Sv, corresponding to the observed range of maximum slope water speed of 3–6 cm s^{-1}. Farther downstream, the NRG injects 12–26 Sv of barotropic flow until 56°W (for a 3–5 cm s^{-1} speed range).

To the south of the GS, the SRG recirculates and infuses mass into the stream both barotropically and baroclinically until 60°W. That barotropic contribution

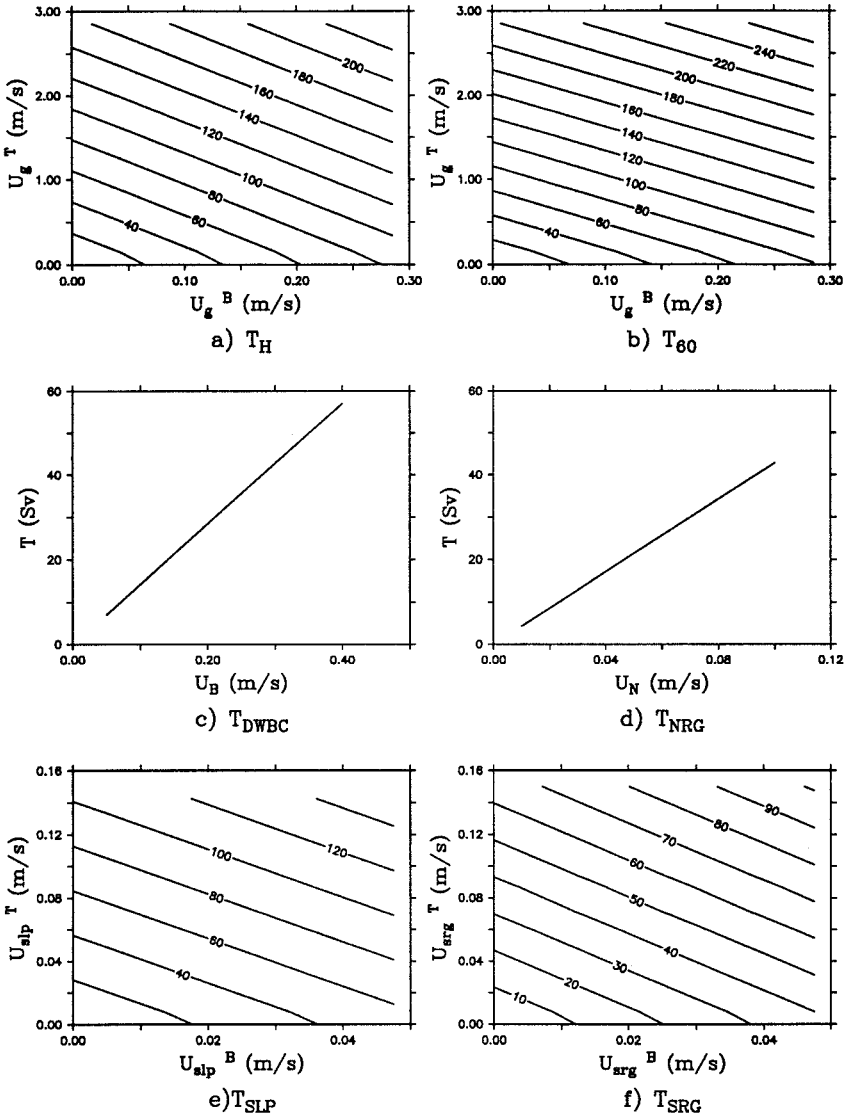

FIG. 12. Transport as a function of top and bottom velocities: (a) Gulf Stream at Cape Hatteras, (b) Gulf Stream at 60°, (c) DWBC, (d) NRG, (e) SLP, and (f) SRG.

is about 24–60 Sv for the possible range of 2–5 cm s^{-1} for the bottom velocity of the gyre. The baroclinic mass influx from this gyre, however, spans a smaller range of 17–34 Sv for the possible top velocity range of 6–10 cm s^{-1}. This is because its effective shear depth is much smaller than the barotropic counterpart, which is the depth of the ocean. Thus, this circulation model depicts a substantial increase of barotropic transport for the GS downstream of Cape Hatteras.

The region from 62° to 56°W is complicated by four factors: (a) mass extraction (both baroclinic and barotropic) to the SRG downstream of 60°W, (b) mass extraction by the SLP baroclinically beyond 62°W, (c) mass injection barotropically from the NRG between 62° and 56°W, and (d) mass injection both barotropically and baroclinically between 62° and 60°W from the SRG to the stream. Thus, it is quite possible that a combination of influx and outflow in this region could make the net transport of the stream remain nearly constant over a longitudinal band such as 60°–56°W, as was observed by Hogg (1992). Note that downstream of 56°W, this circulation model suggests a gradual decrease of transport, both baroclinically and barotropically, that primarily feeds the recirculating gyres to the north and to the south.

So, according to the mass exchange scenario of the multiscale circulation model, it is possible to have a total barotropic mass influx in the range of 36–86 Sv compared to a baroclinic influx of 37–69 Sv into the stream by the surrounding gyres between Cape Hatteras and 60°W. The individual contributions as explained above, are shown in Fig. 11 and listed in Table 4. Thus,

TABLE 4. Range of transport variation.

Feature	Baroclinic (Sv)	Barotropic (Sv)
SRG	17–34	24–60
NRG	—	12–26
SLP	20–35	—
Total addition	37–69	36–86
GS at 60°W	BC + BT	143–225

a typical synoptic GS carrying 70 Sv of transport at Cape Hatteras would have a possible range of 143–225 Sv as its maximum transport at around 60°W, as determined by the choice of the parameters. Clearly, from the observational viewpoint, seasonal variations, mesoscale–jet scale interactions, and large-scale atmospheric forcing of the subbasin-scale gyres govern the real choice of such parameters. What is appealing is that this circulation model would enable one to realize a synoptic three-dimensional field estimate of the western North Atlantic from a very limited number of observations, governed by knowledgeable synthesis and kinematics.

c. Kinematic estimates of transport fluxes into the GS

The synoptic climatology as developed above provides a quantification of transport fluxes from the surrounding gyres into the GS in an average sense. The numbers in the following are evaluated based on the central set of parameters listed in Table 2. Between Cape Hatteras and 73°W, the slope water adds 10 Sv baroclinically, while between 73° and 68°W its contribution is 12 Sv. The SRG contribution is equally partitioned between 10 Sv baroclinic and 10 Sv barotropic. The total transport of 112 Sv at 68°W agrees well with the recent analysis of Johns et al. (1995). In a recent study, Hogg (1992) inferred the transport increase between Cape Hatteras and the Grand Banks as being equally partitioned between the counterrotating gyres to the north and the south. In contrast, in this kinematically balanced climatological state, we find that this increase is unevenly partitioned between the north and the south. In fact, the transport influx from the SRG (46 Sv) is about 1¼ times of that coming in from the north (37 Sv).

Based on the Schmitz (1976) study, the transport addition from SRG is modeled and is almost equally partitioned between baroclinic (22 Sv) and barotropic (24 Sv) components. However, on the cyclonic side of the stream, the baroclinic influx (22 Sv) is only due from the SLP and is about 1.5 times greater than the barotropic influx (15 Sv) from the NRG. This asymmetric influx from the two sides of the stream results in a stream that is relatively more baroclinic on the cyclonic side than it is on the Sargasso side. This asymmetry is further translated in the asymmetric horizontal velocity distribution of the stream in that the stronger shear in the slope water side provides a potential vorticity pool (Johns et al. 1995), whereas the relatively more barotropized Sargasso side provides for an almost uniformly distributed potential vorticity (Leaman et al. 1989) on the average.

It is interesting to note that in a recent analysis, Johns et al. (1995) found that the shift of the subsurface axis from the surface axis increases from 20 km at 73°W to almost 50 km at 55°W in the upper 150–850 m of the GS. This increasing shift or increasing tilt is possibly a signature of increasing baroclinicity of the stream structure that is provided by the increasing influx of baroclinic flow from the surrounding gyres as modeled above from kinematic considerations.

d. The synoptic-stream climatology realization

The climatological mean axis is taken from the mean GS path derived from 12 yr (1975–86) of satellite Advanced Very High Resolution Radiometer data over the western North Atlantic (Gilman 1988). The synoptic GS feature model is put in place on this mean axis along with the SBS gyres in their climatological locations. Although such a configuration is never realized in reality, it provides us with a useful climatology for calibrating and validating regional dynamical models. In Part II, this climatology is used to simulate realistic wavegrowth and meander propagation characteristics and ring formation and absorption behavior. The primitive equation initialization for this synoptic climatology is shown in Fig. 13. The temperature field at 50 m for the multiscale features placed in their mean locations is also shown in Fig. 13. The strength of the DWBC increases as one moves down from a depth of 1800 m (Fig. 13b) to a depth of 3900 m (Fig. 13c). At the bottom (3900 m), the deep GS is primarily formed by the recirculating gyres, and the DWBC follows the 4200-m isobath through the eastern boundary of the domain. The initial adjustment for the GS system at 50 m after 3 days of primitive equation model integration (Fig. 13d) is primarily near the inlet, where the stream and the DWBC readjusts to model dynamics.

5. Construction of synoptic realizations and dynamical adjustment

The kinematically linked velocity distribution for the circulation model is further adjusted to quasigeostrophic (QG) dynamics to yield the physically balanced initialization–assimilation fields. In this section, we first describe the construction of a typical synoptic realization followed by a description of the dynamical adjustment procedure that was used to generate the realization described in section 4d and shown in Fig. 13. As an example of our methodology, a dynamically adjusted nowcast for 21 December 1988 is finally presented.

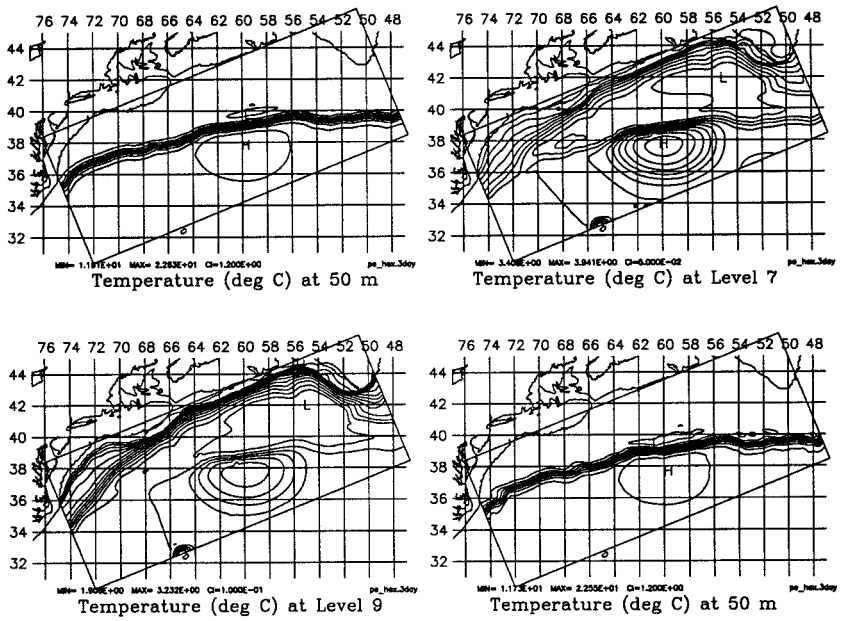

FIG. 13. Primitive equation model initialization and adjustment of the mean state in the GSMR region: (a) initial temperature at 50 m, (b) initial temperature at 1800 m, (c) initial temperature at 3900 m, and (d) 3-day dynamically adjusted temperature at 50 m.

a. Construction and quantification of a typical realization

Initialization of any dynamical model requires the values of each of the prognostic variables at every grid point in the model domain. A typical mesoscale analysis domain in the GSMR region consists of 161 × 65 grid points in the horizontal with 15-km resolution (Robinson et al. 1989). The number of vertical levels typically varies between 6 and 12 depending on the application. Thus, it would require around 10^5 degrees of freedom for each prognostic variable to describe a synoptic state of the ocean.

To quantify the information needed for a MSFM representation, consider setting up a synoptic realization. As described in section 2, the feature models are represented by their three-dimensional velocity fields in terms of horizontal and vertical structures and a few parameters. Once the location of each of these features is identified from various data sources, for example, IR, AXBT, CTD, satellite altimetry, etc., the feature models are located in the model–analysis domain with their various representations. Next, consider the mesoscale variability. For the GS, there are generally six to seven half-meanders in this region, each of which can be specified by three parameters: the span of the meander given by its two crossings of the mean axis and its amplitude. Such a meandering stream axis could be digitized from SST analysis charts produced by NOAA. The velocity structure described in section 2 for the GS is then put in place at the inlet at Cape Hatteras. Meanwhile, the path of the DWBC is modified under the synoptic GS axis location as discussed in section 2a(3). After prescribing the two currents in their synoptic state, the SBS gyres are distorted from their mean state with the constraint of mass conservation (section 2d). Their mean location and geographical extents are preset from observational studies, although one could adjust such parameters if desired. Note that the downstream variation of the GS velocity structure is implemented through the influx and extraction of flow obtained from its interaction with distorted SBS gyres, as explained in section 3c.

Once the velocity fields of the jet-scale currents and the SBS gyres are synthesized kinematically, the mesoscale rings are embedded in the background flow field. The location, size, and strengths of these rings are obtained from SST analysis, satellite altimetry, and/or in situ data, if available. Typically, there are 10–15 rings in this region. Each of the rings is specified by five parameters. So, considering all the features together—that is, the GS, the DWBC, the gyres, and the rings—the MSFM requires about 100 parameter specifications to characterize the synoptic state of the regional circulation. Most of the parameters listed in Table 1—for example, the geographic locations, extents of gyres, DWBC structure, and GS widths—are preset, which reduces the number of degrees of freedom to less than 10 (excluding the GS axis and the rings). In fact, the six independent parameters described in section 3d are the most important ones for the GSMR region. In RG the sensitivity of dynamical models to some of these important parameters is discussed.

Such a collection of velocity field needs to be properly melded, especially at the crossover region and at the

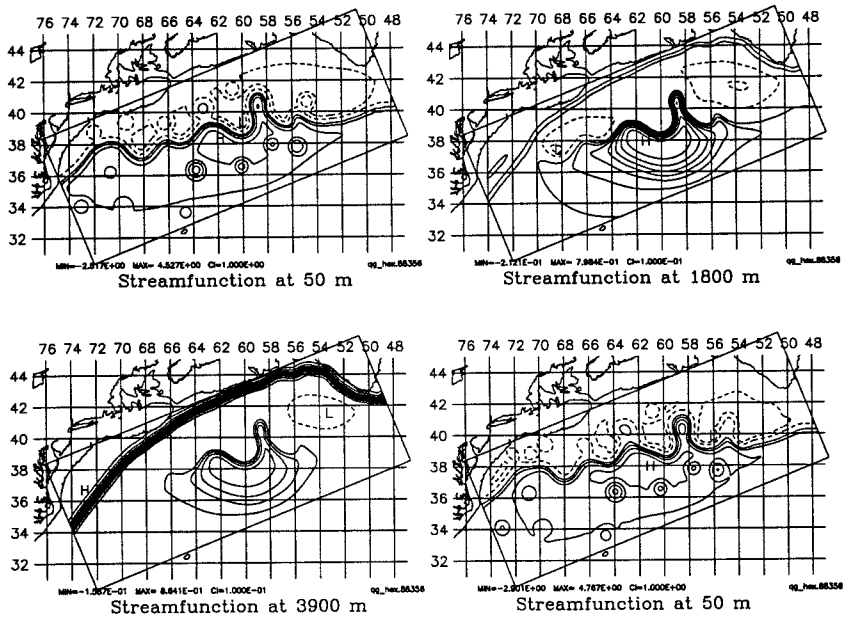

FIG. 14. Quasigeostrophic model initialization and adjustment for the synoptic example: (a) initial streamfunction at 50 m, (b) initial streamfunction at 1800 m, (c) initial streamfunction at 3900 m, and (d) streamfunction at 50 m after 3 days of dynamical simulation.

coastal boundaries. Care is taken not to extend any feature beyond its predefined interaction limit. For example, the flow field of the SRG is restricted to the south of the GS southern edge. Such constraints also allow the superposition of the velocity components in the physical space in such a way that the exponential decay regions of the flow fields of individual features do not introduce spurious noises for other surrounding features. Finally, this ensemble of velocity fields is quasigeostrophically adjusted via the Poisson solver procedure outlined below.

b. *Dynamical adjustment procedure for initialization–assimilation fields*

From the melded three-dimensional kinematically adjusted velocity field, the relative vorticity in the interior is computed as $\zeta_r = \partial v/\partial x - \partial u/\partial y$. A nondivergent boundary streamfunction field is obtained at every level by using a variation of the Hawkins and Rosenthal (1965) approach, which integrates the normal velocity components in a closed loop around the boundary from a single node where the zero (or a known) streamfunction value is prescribed. The closed-loop methodology is necessary to overcome a possible mismatch created by two incoming jets and only one outgoing jet at the deep levels below 800 m. A first-guess streamfunction (ψ_g) field is then obtained by solving the Poisson's equation for the interior streamfunction ($\nabla^2\psi_g = \zeta_r$). Using the known stratification of the model, and from the first-guess streamfunction, the thermal vorticity ζ_t is evaluated and added to the relative vorticity to obtain the potential vorticity ($\zeta_p = \zeta_r + \zeta_t$) in the interior of the domain. The final three-dimensional streamfunction (ψ) field is then obtained by solving the Poisson's equation $\nabla^2\psi = \zeta_p$.

The initialization of the primitive equation model is carried out after a quasigeostrophic dynamical adjustment, which is a type of slow manifold initialization. The 1–3-day QG-adjusted streamfunction field is used to obtain the three-dimensional perturbation density field. This perturbation field is added to the mean density provided by a water-mass model suitable for the GS region (Lozano et al. 1996). This continuous water-mass model projects the density information on a *T–S* plane, which contains the two water types (*T–S* relationship) of the slope and Sargasso regions. Based on the relative proximity of the two water masses from the density observation, the temperature and salinity information are obtained by interpolating along a constant density line using the equation of state.

c. *An example of a synoptic realization*

To represent a specific synoptic realization for the region on 21 December 1988, the stream axis is distorted into its instantaneous position; the northern and southern gyres are correspondingly distorted under the constraint of mass conservation; feature locations and strengths are adjusted according to available synoptic data; and the population of rings is put in place as illustrated in Fig. 14 for a QG model initialization. In Fig. 14a the streamfunction at 50 m (top of the main thermocline) is dominated by the GS and its rings. In the midwater column (Fig. 14b) the SRG is dominant, and in the deep water

(Fig. 14c) the DWBC is also an intense feature. The deep GS is strongest at about 60°W, being created and depleted primarily by barotropic flow from and to the SRG. A 3-day forecast that interacts and dynamically adjusts the features is shown in Fig. 14d. The mesoscale activity of stream–ring interactions has begun; the warm core ring at 63°W is interacting with the stream, and another warm ring at 59°W is beginning to detach from the meander crest. Such (quasigeostrophic) slow manifold representation of the synoptic realization is also often utilized as an initialization field for the PE model.

6. Summary and conclusions

A synthesis of the western North Atlantic circulation has been constructed in terms of a set of feature models for the circulation elements: the GS and deep western boundary currents, the southern and northern recirculation gyres, and the slope water circulation. The feature models are developed by fusing dynamical understanding with information available in historical hydrographic and direct current measurements and previous synthetical studies. The vertical structures of the features are based on averages of typical synoptic observations, whereas the horizontal structures are based on empirical–analytical representations of observational datasets, which approximates the observed potential vorticity distribution well.

Along the axis of the stream, the recirculation gyres inject and extract mass and momentum both barotropically and baroclinically, the mechanism of which has been kinematically modeled in terms of multiscale interaction parameters. The geographical distribution of the structures then provides a set of consistency conditions among the feature model parameters. Such kinematically mass balanced conditions are consistent with values of individual feature model parameters in the realistic observational range.

Using observational studies listed in Table 1, a central set of parameter values for the synoptic structures of the permanent fronts and the mean state gyres has been selected (see Table 2) for a particular kinematic synthesis that yields a synoptic-stream climatology of the western North Atlantic. This realization provides a GS whose along-stream transport variation matches well with past observations at 73°, 68°, and 60°W. The asymmetric transport influx as obtained via the synthesis may be the reason for the observed asymmetry in the velocity distribution and the along-stream increase in the offshore tilt of the stream.

Finally, a robust and stable methodology for obtaining a synoptic initialization–assimilation field for a generic primitive equation model is established. Synoptic realizations via multiscale feature models, utilizing primarily preset parameter values, require only a limited number of degrees of freedom (<50) to prescribe the initialization or assimilation field for a 10^5 gridpoint domain. An example field for a dynamically adjusted nowcast is shown here, and its successful dynamical evolution will be discussed in detail in Part III (Gangopadhyay and Robinson 1997).

Acknowledgments. This study was supported by the Office of Naval Research (N00014-93-I-0577 and N00014-90-J-1612) through contracts to Harvard University. Preliminary simulations were carried out at San Diego Supercomputer Center and at LSC at Stennis Space Center. Special thanks to Dr. W. Johns at University of Miami and Tom Rossby at URI for providing the Pegasus dataset. We are grateful to Dr. Carlos Lozano for his helpful discussions on numerical modeling issues. We would also like to thank Ms. Marsha Cormier, Mr. Wayne G. Leslie, and other members of the Harvard University Oceanography group for their support to this work at numerous instances. AG had completed the revised version of the manuscript under a NASA Grant 944-47172-0-3237 while at JPL, with support from Dr. Lee Fu. Lastly, we thank two anonymous reviewers and Dr. Ichiro Fukumori for some helpful suggestions regarding the presentation of the manuscript.

APPENDIX

Feature Model Structures

The nondimensional horizontal and vertical velocity profiles for the different features are defined as follows.

(a) $\gamma_{GS}(y)$:

$$\gamma_{GS}(y) = \begin{cases} e^{-y^2}/g_n^2, \\ \quad \text{for } 0 \le y \le g_n \\ ay + be^{y/l_1} + c, \\ \quad \text{for } -g_1 \le y \le 0 \\ a_1(-y - g_2 + g_1) + b_1 e^{(y-g_1)/l_2}, \\ \quad \text{for } -g_2 \le y \le -g_1, \end{cases} \tag{A1}$$

where g_n is the width of the GS on the slope water side; g_1 and g_2 are shown in Fig. 2c; l_1 and l_2 are the e-folding scales for the exponentials used to maintain continuity of slopes at $y = 0$ and $y = -g_1$.

The free parameters of the distribution are the GS widths g_1, g_2, and g_n, and the e-folding length scales l_1 and l_2. The dependent parameters a, b, c, a_1, and b_1 are defined by

$$\begin{aligned} a &= \frac{(1 - r + sl_1)}{g_1}, \\ b &= -al_1, \\ c &= 1 - b \\ s &= \frac{1 - r}{g_1}, \\ a_1 &= \frac{sl_2 - r}{g_2 + l_2}, \\ b_1 &= l_2(s - a_1). \end{aligned} \tag{A2}$$

Note that in Fig. 2c, the axis velocity is u_a and the velocity at the break between the two linear segments is given by u_s, and $r = u_s/u_a$. At any depth, the axis velocity $u_a(x, z) = (U_x^T - U_x^B)\phi(x, z) + U_x^B$. Clearly, at the surface, where $\phi(x, 0) = 1$, $u_a(x, 0) = U_x^T$, and at the bottom, where $\phi(x, -H) = 0$, $u_a(x, -H) = U_x^B$.

(b) $\gamma_{\text{SRG}}(r)$ and $\phi_{\text{SRG}}(z)$:

Here $\gamma_{\text{SRG}}(r)$ increases linearly to a distance $r_m/2$ ($r_m^2 = a^2 \cos^2\alpha + b^2 \sin^2\alpha$), then it decays exponentially to the outer boundary and vanishes outside the gyre as given by

$$\gamma_{\text{SRG}}(r) = \begin{cases} \dfrac{2r}{r_m}, & \text{for } r \le r_m/2 \\ e^{4(1-2r/r_m)}, & \text{for } r_m/2 < r \le r_m \\ 0, & \text{for } r > r_m: \end{cases} \quad \text{(A3)}$$

$$\phi_{\text{SRG}}(z) = \frac{\Delta D_{\text{SAR}}(z) - \Delta D_{\text{SAR}}(-H)}{\Delta D_{\text{SAR}}(0) - \Delta D_{\text{SAR}}(-H)}. \quad \text{(A4)}$$

(c) The feature model horizontal velocity distribution for the NRG is

$$\gamma_{\text{NRG}}(r) = \begin{cases} \dfrac{r_p}{r_m}, & \text{for } r_p \le r_m \\ e^{3(1-r_p/r_m)}, & \text{for } r_p > r_m, \end{cases} \quad \text{(A5)}$$

where r_m is the distance of the maximum radial velocity of the ellipse defined in (b) above:

(d)

$$\gamma_{\text{SLP}}(r) = \begin{cases} \dfrac{r}{r_m}, & \text{for } r \le r_m \\ 0, & \text{for } r > r_m. \end{cases} \quad \text{(A6)}$$

$$\phi_{\text{SLP}}(z) = \frac{\Delta D_{\text{SLP}}(z) - \Delta D_{\text{SLP}}(-H)}{\Delta D_{\text{SLP}}(0) - \Delta D_{\text{SLP}}(-H)}. \quad \text{(A7)}$$

REFERENCES

Arango, H. A., A. Gangopadhyay, and A. R. Robinson, 1992: Feature models for the western North Atlantic: Currents, subbasin, and mesoscale features in the GSMR region. Rep. in Meteorology and Oceanography 43, Harvard University, Cambridge, MA, 60 pp. [Available from Division of Applied Sciences, Harvard University, Cambridge, MA 02138.]

Bane, J. M., Jr., O. B. Brown, and R. H. Evans, 1988: Gulf Stream remote forcing of shelf-break currents in the mid-Atlantic bight. *Geophys. Res. Lett.,* **15,** 405–407.

Bisagni, J. J., and P. Cornillon, 1984: The synoptic sound-speed field of a warmcore GS ring. *J. Acoust. Soc. Amer.,* **76,** 532–539.

Brown, O. B., P. Cornillon, S. R. Emmerson, and H. M. Carle, 1986: Gulf Stream warm rings: A statistical study of their behavior. *Deep-Sea Res.,* **33,** 1459–1473.

Churchill, J. H., and P. C. Cornillon, 1991: GS water on the shelf and upper slope north of Cape Hatteras. *Cont. Shelf Res.,* **11,** 409–431.

Clancy, R. M., P. A. Phoebus, K. D. Pollack, and J. Cummings, 1990: Operational global scale ocean thermal analysis system. *J. Atmos. Oceanic Technol.,* **7,** 233–254.

Cornillon, P. C., R. Weyer, and G. Flierl, 1989: Translational velocity of warm core rings relative to the slope water. *J. Phys. Oceanogr.,* **19,** 1317–1332.

Flierl, G. R., 1977: The application of linear quasigeostrophic dynamics to the GS rings. *J. Phys. Oceanogr.,* **7,** 365–379.

Fox, D. N., M. R. Carnes, and J. L. Mitchell, 1993: Circulation model experiments of the Gulf Stream using satellite derived fields. Naval Research Laboratory Formal Rep. NRL/FR/7323-92-9412, Stennis Space Center, MS, 45 pp. [Available from NRL-Stennis, Stennis Space Center, MS 39529.]

Gangopadhyay, A., and A. R. Robinson, 1997: Circulation and dynamics of the western North Atlantic. Part III: Forecasting the meanders and rings. *J. Atmos. Oceanic Technol.,* **14,** 1352–1365.

Gilman, C., 1988: A study of the GS downstream of Cape Hatteras, 1975–1986. M.S. thesis, University of Rhode Island, 75 pp. [Available from University of Rhode Island, Kingston, RI 02881.]

Glenn, S. M., and A. R. Robinson, 1995: Validation of an operational Gulf Stream forecasting model. *Qualitative Skill Assessment for Coastal Models,* AGU Estuarine/Coastal Series, Vol. 47, American Geophysical Union, 469–499.

Halkin, D., and H. T. Rossby, 1985: The structure and transport of the GS at 73°W. *J. Phys. Oceanogr.,* **15,** 1439–1452.

Hall, M. M., and H. L. Bryden, 1985: Profiling the GS with a current meter mooring. *Geophys. Res. Lett.,* **12,** 203–206.

Hawkins, H. F., and S. L. Rosenthal, 1965: On the computation of streamfunctions from the wind field. *Mon. Wea. Rev.,* **93,** 245–252.

Hogg, N. G., 1983: A note on the deep circulation of the western North Atlantic: its nature and causes. *Deep-Sea Res.,* **30,** 945–961.

——, 1992: On the transport of the GS between Cape Hatteras and the Grand Banks. *Deep-Sea Res.,* **39,** 1231–1246.

——, and H. Stommel, 1985: On the relationship between the deep circulation and the GS. *Deep-Sea Res.,* **32,** 1181–1193.

——, R. S. Pickart, R. M. Hendry, and W. J. Smethie Jr., 1986: The northern recirculation gyre of the GS. *Deep-Sea Res.,* **33,** 1139–1165.

Hurlburt, H. E., 1986: Dynamic transfer of simulated altimeter data into subsurface information by a numerical ocean model. *J. Geophys. Res.,* **91,** 2372–2400.

——, D. N. Fox, and E. J. Metzger, 1990: Statistical inference of weakly-correlated subthermocline fields from satellite altimeter data. *J. Geophys. Res.,* **95,** 11 375–11 409.

Johns, W. E., T. J. Shay, J. M. Bane, and D. R. Watts, 1995: Gulf Stream structure, transport, and recirculation near 68°W. *J. Geophys. Res.,* **100,** 817–838.

Knauss, J. A., 1969: A note on the transport of the GS. *Deep-Sea Res.,* **16** (Suppl.), 117–123.

Lai, D. Y., and P. L. Richardson, 1977: Distribution and movement of GS rings. *J. Phys. Oceanogr.,* **7,** 670–683.

Leaman, K. D., E. Johns, and H. T. Rossby, 1989: The average distribution of volume transport and potential vorticity with temperature at three sections across the Gulf Stream. *J. Phys. Oceanogr.,* **19,** 36–51.

Levitus, S., 1982: Climatological atlas of the world ocean. NOAA Professional Paper 13, U.S. Govt. Printing Office, 173 pp.

Lozano, C. J., A. R. Robinson, H. G. Arango, A. Gangopadhyay, Q. Sloan, P. J. Haley, and W. G. Leslie, 1996: An interdisciplinary ocean prediction system: Assimilation strategies and structured data models. *Modern Approaches to Data Assimilation on Ocean Modeling,* P. Malanotte-Rizzoli, Ed., Elsevier Oceanography Series, Elsevier Science, 413–452.

McWilliams, J. C., and G. R. Flierl, 1979: On the evolution of isolated, nonlinear vortices. *J. Phys. Oceanogr.,* **9,** 1155–1182.

Niiler, P. P., and A. R. Robinson, 1967: The theory of free inertial jets: II. A numerical experiment for the path of the Gulf Stream. *Tellus,* **19** (4), 601–619.

Olson, D. B., 1980: The physical oceanography of two rings observed by the Cyclonic Ring Experiment. Part II: Dynamics. *J. Phys. Oceanogr.,* **10,** 514–528.

Pickart, R. S., 1992a: Water mass components of the North Atlantic deep western boundary current. *Deep-Sea Res.*, **39,** 1553–1572.

——, 1992b: Space–time variability of the deep western boundary current oxygen core. *J. Phys. Oceanogr.,* **22,** 1047–1061.

——, and N. G. Hogg, 1989: A tracer study of the deep Gulf Stream cyclonic recirculation. *Deep-Sea Res.,* **36,** 935–956.

——, and D. R. Watts, 1990: Deep western boundary current variability at Cape Hatteras. *J. Mar. Res.,* **48,** 765–791.

——, and W. M. Smethie Jr., 1993: How does the deep western boundary current cross the Gulf Stream? *J. Phys. Oceanogr.*, **23,** 2602–2616.

Richardson, P. L., 1985: Average velocity and transport of the Gulf Stream near 55°W. *J. Mar. Res.,* **43,** 83–111.

——, and J. A. Knauss, 1971: Gulf Stream and western boundary undercurrent observations at Cape Hatteras. *Deep-Sea Res.,* **18,** 1089–1109.

Robinson, A. R., and A. Gangopadhyay, 1997: Circulation and dynamics of the western North Atlantic. Part II: Dynamics of meander and rings. *J. Atmos. Oceanic Technol.,* **14,** 1333–1351.

——, J. R. Luyten, and F. C. Fuglister, 1974: Transient GS meandering. Part I: An observational experiment. *J. Phys. Oceanogr.*, **4,** 237–255.

——, M. A. Spall, and N. Pinardi, 1988: GS simulations and the dynamics of ring and meander processes. *J. Phys. Oceanogr.*, **18,** 1811–1853.

——, S. M. Glenn, M. A. Spall, L. J. Walstad, G. M. Gardner, and W. G. Leslie, 1989: Forecasting GS meanders and rings. *EOS, Oceanogr. Rep.,* **70** (45), 1464–1473.

Schmitz, W. J., Jr., 1976: Eddy kinetic energy in the deep western North Atlantic. *J. Geophys. Res.,* **81,** 4981–4982.

Spall, M. A., and A. R. Robinson 1990: Regional primitive equation studies of the GS meander and ring formation region. *J. Phys. Oceanogr.,* **20,** 985–1016.

Stommel, H. M., 1957: A survey of ocean current theory. *Deep-Sea Res.,* **4,** 149–184.

Swallow, J. C., and L. V. Worthington, 1961: An observation of a deep counter-current in the western North Atlantic. *Deep-Sea Res.,* **8,** 1–19.

Volkman, G. H., 1962: Deep current observations in the western North Atlantic, *Deep-Sea Res.*, **9,** 493–500.

Watts, D. R., 1985: Gulf stream variability. *Eddies in Marine Science,* A. R. Robinson, Ed., Springer-Verlag, 114–144.

Worthington, L V., 1976: On the North Atlantic circulation. *The Johns Hopkins Oceanographic Studies Monogr.*, No. 6, The Johns Hopkins University Press, 110 pp.